# Acoustically driven magnons in CrSBr bilayers

Anton Shubnic [1,*] Igor Chestnov [1] Igor Lobanov [1] Valery Uzdin [1] Ivan Iorsh [1,2,†] and Ivan A. Shelykh [3,‡]

[1]*Department of Physics, ITMO University, Saint Petersburg 197101, Russia*

[2]*Department of Physics, Engineering Physics and Astronomy, Queen's University, Kingston, Ontario K7L 3N6, Canada*

[3]*Science Institute, University of Iceland, Dunhagi 3, IS-107 Reykjavik, Iceland*

(Received 13 April 2026; accepted 16 September 2026; published 6 November 2026)

We study the coupling between spin excitations and acoustic waves in bilayers of CrSBr, an ambiently stable two-dimensional (2D) magnetic material. We demonstrate that a strong dependence of interlayer exchange coupling on strain makes possible the resonant generation of magnons by an acoustic wave. It is shown that the parameters of the generation, in particular, the resonant frequency, can be tuned by an external magnetic field, which makes CrSBr a promising platform for spintronics applications.

DOI: 10.1103/xdkq-h9km

## I. INTRODUCTION

Since the discovery of graphene [1], the physics of two-dimensional (2D) materials has evolved in a rapidly developing field with prospects for applications in nanoelectronics. Layered van der Waals materials are characterized by strong light-matter [2] and spin-orbit interactions [3], which makes them prominent candidates for optoelectronic and spintronics applications. For a long time, the question of the existence of magnetic two-dimensional materials remained open until $CrI_3$ [4], an Ising ferromagnet with a Curie temperature of ≈45 K and possessing a set of outstanding properties, such as giant tunneling magnetoresistance [5], magnetoelectric coupling [6], magnetic second harmonic generation [7] and excitonic Rabi splitting [8] was experimentally discovered. Unfortunately, this material is unstable under ambient conditions as it is subject to fast oxidation and hydration processes, which seriously limit the range of its possible applications [9].

Recently, an air-stable 2D material, namely, CrSBr, was discovered. Possessing an orthorhombic symmetry, this material is characterized by two nonequivalent crystallographic directions and demonstrates a strong anisotropy of its optical [10], electronic [11] and magnetic [12] properties. In monolayer geometry, it is a ferromagnet with Curie temperature of about 140 K [13]. In multilayer configuration, the intralayer ferromagnetic (FM) order coexists with the antiferromagnetic (AFM) interlayer coupling [14], so that in the zero external magnetic field the net magnetization remains zero.

One of the key features of 2D magnetic materials is the possibility of tuning of their magnetic properties by external strains. For example, applying strain to the $MoN_2$ monolayer, it is possible to achieve a phase transition accompanied by switching the magnetic order from FM to AFM [15]. A pronounced magnetomechanical response has also been observed in CrSBr [16–19]. In particular, recent experimental [20] and theoretical [21] studies have shown that the uniaxial strain applied along the crystallographic *a* axis dramatically modifies the interlayer exchange, driving a transition from the AFM to FM phase. This strong magnetoelastic coupling opens new avenues for exploring novel magnetomechanical effects in CrSBr.

Magnetoelastic interactions between magnons and phonons have been studied since the pioneering works of Kittel [22,23]. CrSBr supports long-lived magnons in both bulk samples and bilayers [24], as well as additional surface magnon modes in bulk crystals [25]. Recent time-resolved experiments have demonstrated that transient strain fields associated with out-of-plane transverse and in-plane longitudinal lattice displacements can launch coherent magnon wave packets in CrSBr [26]. The generation of coherent acoustic phonons by femtosecond laser pulses [27] and their coupling to magnons [28] have also been demonstrated in bulk CrSBr. However, the role of the magnetic configuration in governing this dynamical coupling remains to be clarified.

In this article, we develop a microscopic theory of acoustically driven magnon generation in CrSBr bilayers and demonstrate the possibility of resonant excitation of GHz magnons by an external acoustic wave due to the time-periodic modulation of the interlayer exchange. We show that the coupling strength between magnons and phonons is proportional to the cross product of the Neel and net magnetization vectors. Consequently, an external out-of-plane magnetic field is required to activate this coupling. We further show that the generation frequency, amplitude, and resonance half-width depend on the external magnetic field, highlighting the potential of CrSBr bilayers for precisely controllable spintronic devices.

*Contact author: anton.shubnic@metalab.ifmo.ru

†Contact author: ivan.iorsh@queensu.ca

‡Contact author: shelykh@hi.is

*Published by the American Physical Society under the terms of the Creative Commons Attribution 4.0 International license. Further distribution of this work must maintain attribution to the author(s) and the published article's title, journal citation, and DOI.*

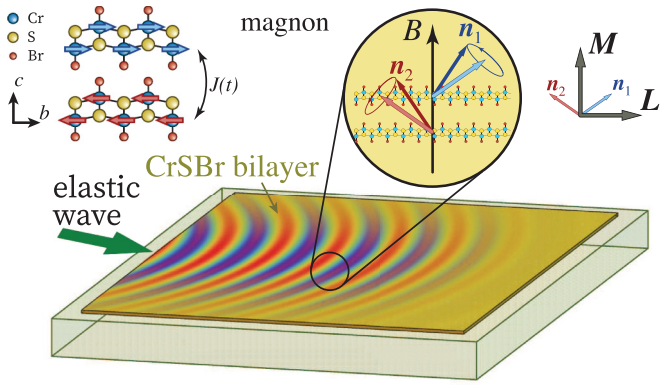



FIG. 1. The geometry of the proposed device for resonant acoustic generation of magnons in CrSBr bilayer. An acoustic wave produces the in-plane strain in the CrSBr (color coded), which modulates the interlayer magnetic exchange parameter $J$. A periodic change in $J$ leads to the generation of a spin wave. The coupling strength between magnons and phonons is proportional to the cross product of the Neel and net magnetization vectors, so the application of an external out-of-plane magnetic field is necessary.

## II. MODEL

We consider a bilayer of CrSBr as sketched in Fig. 1. The stable magnetic configuration of the system can be obtained by minimization of the following energy functional [24]:

$$E_0 = \int \mathrm{d}^2\boldsymbol{r}\Big[\hat{D}[\boldsymbol{n}_1] + \hat{D}[\boldsymbol{n}_2] + \frac{K_c}{2}\left(n_{1c}^2 + n_{2c}^2\right) + \frac{K_a}{2}\left(n_{1a}^2 + n_{2a}^2\right) + J\boldsymbol{n}_1\boldsymbol{n}_2 - B(n_{1c} + n_{2c})\Big],$$
$$\hat{D}[\boldsymbol{n}] = A_a\left(\frac{\partial \boldsymbol{n}}{\partial a}\right)^2 + A_b\left(\frac{\partial \boldsymbol{n}}{\partial b}\right)^2, \tag{1}$$

where $\boldsymbol{n}_1$ and $\boldsymbol{n}_2$ are the magnetization unit vectors of the upper and lower layers, respectively; $J \equiv J(t)$ is the interlayer exchange constant, sensitive to a local strain created by the elastic wave; $B$ is the external magnetic field applied along the hard axis $c$; and $K_c$ and $K_a$ are single-ion anisotropies in $c$ and $a$ crystallographic directions. Here, we use $K_c = 0.9\,\mathrm{meV/nm^2}$, $K_a = 0.55\,\mathrm{meV/nm^2}$, and $J = 0.076\,\mathrm{meV/nm^2}$ [24] in the equilibrium. Here, we took into account that the effective interlayer magnetic exchange in the bilayer is twice as low as in a bulk. In addition, using the intralayer exchange coupling constants $J_a = 3.22\,\mathrm{meV}$, $J_b = 2.78\,\mathrm{meV}$, and $J_{ab} = 4.11\,\mathrm{meV}$ from Ref. [29] we obtain the following values for the intralayer exchange parameters: $A_a = 8.73\,\mathrm{meV}$ and $A_b = 14.78\,\mathrm{meV}$ in the continuum limit (see the Supplemental Material [30]).

The spin dynamics is described by a set of Landau-Lifshitz-Gilbert (LLG) equations:

$$\frac{\partial \boldsymbol{n}_1}{\partial t} = \frac{\gamma_0}{n_s}\left[\boldsymbol{n}_1 \times \frac{\delta E_0}{\delta \boldsymbol{n}_1}\right] + \alpha\left[\boldsymbol{n}_1 \times \frac{\partial \boldsymbol{n}_1}{\partial t}\right],$$
$$\frac{\partial \boldsymbol{n}_2}{\partial t} = \frac{\gamma_0}{n_s}\left[\boldsymbol{n}_2 \times \frac{\delta E_0}{\delta \boldsymbol{n}_2}\right] + \alpha\left[\boldsymbol{n}_2 \times \frac{\partial \boldsymbol{n}_2}{\partial t}\right], \tag{2}$$

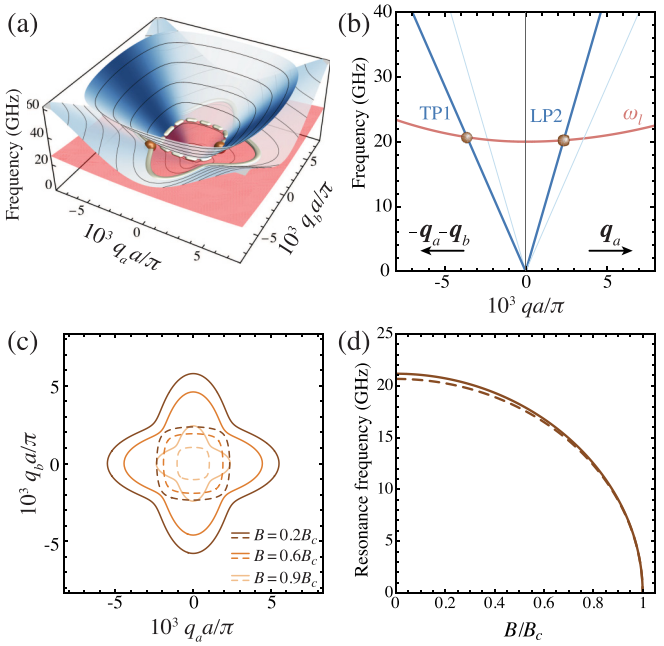



FIG. 2. (a) Magnon and phonon dispersions in a CrSBr bilayer. The blue surfaces correspond to the lower $\Omega_{P1}$ and upper $\Omega_{P2}$ acoustic waves (6). The color saturation represents the normalized magnetoelastic driving efficiency, $\eta = |\varepsilon_{aa}|^2/(q^2|\boldsymbol{u}_0|^2) = q_a^2|u_{0a}|^2/(q^2|\boldsymbol{u}_0|^2)$, where $u_a$ stands for the projection of the displacement vector $\boldsymbol{u}_0$ onto the $a$ axis. The red surface corresponds to the $l_\perp$ magnon mode at $B = 0.2B_c$. The resonance conditions are shown with the gray solid and dashed lines. The points of the most efficient generation are shown by brown dots. (b) The cross section of the dispersion from panel (a) around the Γ-point. Magnons and phonons propagating in the $a$ direction are shown on the right of the Γ point, while the left side corresponds to propagation with $-\boldsymbol{q}_a - \boldsymbol{q}_b$. The transverse TP1 and the longitudinal LP2 phonon modes with maximal $a$ component of the displacement magnitude $\boldsymbol{u}_0$ are shown with saturated blue color, while the other phonon states are shown with the pale shade. The resonances at the intersection of the magnon (red) and the phonon branches are indicated with brown dots. (c) The resonance cross sections in the momentum space at various magnetic fields. The solid lines indicate the intersection with the lower phonon mode $\Omega_{P1}$, while the dashed lines stand for the $\Omega_{P2}$ resonance. (d) The dependence of resonant generation frequency corresponding to the dots in panels (a) and (b) on external magnetic field. The solid curve corresponds to the resonance with the TP1 phonon mode, while the dashed one stands for the LP2 resonance.

where $\gamma_0/2\pi = 28$ GHz/T and $\alpha = 0.066$ are correspondingly the gyromagnetic ratio and the Gilbert damping constant [24,31]; $n_s = (3/2)\mu_B/(a_0 b_0/2)$ is a saturation magnetization, where $\mu_B$ is the Bohr magneton, $a_0 = 0.351$ nm, and $b_0 = 0.477$ nm are the lattice constants [32], and we take into account the presence of two Cr atoms in a unit cell with three electrons in each atom.

Let us introduce the total magnetization $\boldsymbol{M} = \boldsymbol{n}_1 + \boldsymbol{n}_2$ and the Neel $\boldsymbol{L} = \boldsymbol{n}_1 - \boldsymbol{n}_2$ vectors. At zero magnetic field, the bilayer is in the AFM state $M = 0$ and $\boldsymbol{L} = 2\boldsymbol{e}_b$. The canted phase (see Fig. 1) with $\boldsymbol{M} = 2B/(2J + K_c)\boldsymbol{e}_c$ and $\boldsymbol{L} = \sqrt{4 - M^2}\boldsymbol{e}_b$ is realized at $B < B_c$, where $B_c = 2J + K_c$ is the critical field corresponding to the transition to the FM phase.

To determine the magnon dispersion in the CrSBr bilayer, we linearize the LLG equations (2) by the spin-wave ansatz: $\boldsymbol{M} = \boldsymbol{M}_0 + \boldsymbol{m}e^{i(\omega t - \boldsymbol{qr})}$ and $\boldsymbol{L} = \boldsymbol{L}_0 + \boldsymbol{l}e^{i(\omega t - \boldsymbol{qr})}$, and investigate the evolution of weak excitations $\boldsymbol{m}$ and $\boldsymbol{l}$ around the equilibrium values $\boldsymbol{M}_0$ and $\boldsymbol{L}_0$. Using the relations $\boldsymbol{ML} = 0$ and $\boldsymbol{M}^2 + \boldsymbol{L}^2 = 4$, which follows from the normalization conditions, reduces the problem to the decoupled evolution of the in-plane magnetization $\boldsymbol{m}_\perp = (m_a, m_b)$ and Neel vector $\boldsymbol{l}_\perp = (l_a, l_b)$ components:

$$\frac{dm_a}{dt} = C^m_{ab} m_b - \Gamma^m_a m_a,$$
$$\frac{dm_b}{dt} = -C^m_{ba} m_a - \Gamma^m_b m_b, \tag{3a}$$
$$\frac{dl_a}{dt} = C^l_{ab} l_b - \Gamma^l_a l_a,$$
$$\frac{dl_b}{dt} = -C^l_{ba} l_a - \Gamma^l_b l_b, \tag{3b}$$

where

$$C^m_{ab} = \frac{\gamma}{M_0}\left[(D(\boldsymbol{q}) + J)M_0^2 + \left(D(\boldsymbol{q}) + \frac{K_c}{2}\right)L_0^2\right],$$
$$C^m_{ba} = \gamma\left(D(\boldsymbol{q}) + J + \frac{K_a}{2}\right)M_0,$$
$$C^l_{ab} = \frac{\gamma}{M_0}\left[D(\boldsymbol{q})M_0^2 + \left(D(\boldsymbol{q}) + J + \frac{K_c}{2}\right)L_0^2\right],$$
$$C^l_{ba} = \gamma\left(D(\boldsymbol{q}) + \frac{K_a}{2}\right)M_0,$$

and the damping parameters are $\Gamma^j_a = 2\alpha C^j_{ba}/M_0$ and $\Gamma^j_b = \alpha C^j_{ab} M_0/2$ with $j = m, l$. Here, we introduced the effective gyromagnetic ratio $\gamma = (\gamma_0/n_s)/(1+\alpha^2)$ and defined the in-plane exchange part of the dispersion $D(\boldsymbol{q}) = A_a q_a^2 + A_b q_b^2$.

In accordance with previously accepted notations [24,33], we recognize the $\boldsymbol{m}_\perp$ mode governed by Eq. (3a) as the out-of-phase magnon state, for which the excitations of the layer magnetization vectors point in opposite directions, while the $\boldsymbol{l}_\perp$ mode is the in-phase (IP) magnon. The dispersion of these states reads

$$\omega_j = \sqrt{C^j_{ab}C^j_{ba} - \frac{\left(\Gamma^j_a - \Gamma^j_b\right)^2}{4}} + i\frac{\Gamma^j_a + \Gamma^j_b}{2}. \tag{4}$$

In the following, we focus on the $\boldsymbol{l}_\perp$ mode, whose dispersion is shown in red in Figs. 2(a) and 2(b). The $\boldsymbol{m}_\perp$ mode remains decoupled from the elastic waves due to the specific symmetry of the magnetoelastic interaction in CrSBr. The interlayer exchange energy, $J\boldsymbol{n}_1\boldsymbol{n}_2$, generates torques in the adjacent layer magnetizations that are equal in magnitude but opposite in direction: $\partial_t \boldsymbol{n}_{1,2} \propto \pm J[\boldsymbol{n}_1 \times \boldsymbol{n}_2]$. Consequently, within the linearized model, phonon-induced modulation of interlayer coupling does not excite in-plane net magnetization, leaving the $\boldsymbol{m}_\perp$ mode inactive.

The dispersion relation for phonons and their polarization can be obtained from the following equation for in-plane atomic displacements $\boldsymbol{u}$:

$$\rho\frac{\partial^2 u_i}{\partial t^2} = C_{ijkl}\frac{\partial^2 u_l}{\partial x_j \partial x_k}, \tag{5}$$

where $\rho$ is the material density and $C_{ijkl}$ are the components of the elasticity tensor, symmetric in the permutation of the last two indices. The following nonzero values of the $\hat{C}$ tensor for an orthorhombic crystal (in Voigt notation), $C_{11} = 141$ GPa, $C_{22} = 142$ GPa, $C_{12} = 17.5$ GPa, and $C_{66} = 28$ GPa, were obtained by us using DFT calculations (see the Supplemental Material [30]). In what follows, we restrict our analysis to long-wavelength in-plane acoustic phonon modes described by a common displacement field $\mathbf{u}$. We further assume that the bilayer is located on a rigid substrate. The complete phonon spectrum of a CrSBr bilayer also contains interlayer shear and breathing modes, as well as higher optical branches [34]. These modes are not included in the present continuum description and may provide additional magnetoelastic coupling channels. Under these assumptions, Eq. (5) with $\boldsymbol{u} = \boldsymbol{u}_0 e^{i(\boldsymbol{qr} - \omega t)}$ yields two acoustic branches:

$$\Omega^2_{\mathrm{P1,P2}} = \frac{1}{2\rho}\Big[(C_{11} + C_{66})q_a^2 + (C_{22} + C_{66})q_b^2 \mp \sqrt{\left((C_{11} - C_{66})q_a^2 - (C_{22} - C_{66})q_b^2\right)^2 + 4(C_{12} + C_{66})^2 q_a^2 q_b^2}\Big], \tag{6}$$

shown in Fig. 2(a) with the blue color. The colormap encodes magnetoelastic driving efficiency associated with $\varepsilon_{aa} = \partial u_a/\partial a = iq_a u_a$, the only strain component that modulates the interlayer exchange [20]. Therefore, magnons are excited most efficiently by the upper-branch longitudinal phonon (LP2) propagating along the $a$ axis. The lower branch is predominantly transverse and decouples from magnons along both principal axes: $u_a = 0$ for propagation along $a$, whereas $q_a = 0$ for propagation along $b$. Away from the principal axes, polarization mixing enables coupling to the lower branch. We consider propagation along the negative diagonal and denote the corresponding resonance as TP1 [see Figs. 2(a) and 2(b)].

The efficient excitation requires matching of both energy and momentum between magnons and phonons. This matching occurs at the intersections of their dispersion surfaces, as illustrated in Figs. 2(a) and 2(b), for the cross sections along the $\boldsymbol{q}_a$ (right, LP2 phonon) and $-\boldsymbol{q}_a - \boldsymbol{q}_b$ (left, TP1 phonon) directions.

The resulting resonance conditions form intricate contours in the wave vector plane, as shown in Fig. 2(c), where solid and dashed lines correspond to resonances with the lower ($\Omega_{P1}$) and upper ($\Omega_{P2}$) branches, respectively. The shape and position of these contours are highly sensitive to the external magnetic field, enabling precise tuning of the energy and momentum of the generated magnons. The magnetic field

dependencies of magnon frequencies at the TP1 and LP2 resonances are shown in Fig. 2(d) with the solid and dashed lines, respectively.

Note that in addition to the resonances shown in Fig. 2, additional intersections between the magnon and phonon dispersions occur in the subterahertz frequency range. We do not consider these resonances in this work, as generation of terahertz phonons is experimentally challenging.

To quantify the phonon-magnon coupling strength, we consider a weak periodic modulation of the interlayer coupling constant induced by the elastic wave: $J(t) = J_0 + W(t)$. For small strains around the equilibrium state, we retain only the leading linear variation of $J$ with strain. Therefore, $W(\mathbf{r}, t)$ follows the local strain produced by the acoustic wave. The Neel vector then acquires an additional time-dependent torque $2W(t)[\boldsymbol{n}_1 \times \boldsymbol{n}_2] = W(t)[\boldsymbol{L} \times \boldsymbol{M}]$. To leading order, $\boldsymbol{M} \approx M_0 \boldsymbol{e}_c$ and $\boldsymbol{L} = L_0 \boldsymbol{e}_b$, so this term acts as a driving force applied along the $a$ direction. Equation (3b) thus corresponds to one of a driven harmonic oscillator:

$$\frac{dl_a}{dt} = C^l_{ab} l_b - \Gamma^l_a l_a + \gamma W(\boldsymbol{r}, t) M_0 L_0,$$
$$\frac{dl_b}{dt} = -C^l_{ba} l_a - \Gamma^l_b l_b. \tag{7}$$

Note that the driving term exists only in the canted phase, where both $M_0$ and $L_0$ are nonzero, and vanishes in the collinear FM and AFM phases.

In what follows, we consider the driving acoustic wave $W(\boldsymbol{r}, t) = W_0 \cos(\boldsymbol{q}r - \Omega t)$ propagating with the wave vector $\boldsymbol{q}$ and frequency $\Omega \equiv \Omega(\boldsymbol{q})$ given by Eq. (6). Placing $(l_a, l_b)^T = C_1(t)\boldsymbol{A}_1 \exp(\lambda_1 t) + C_2(t)\boldsymbol{A}_2 \exp(\lambda_2 t)$ into Eq. (7), where $C_{1,2}(t)$ are unknown functions, $\boldsymbol{A}_{1,2}$ and $\lambda_{1,2}$ are the eigenvectors and eigenvalues of the characteristic matrix

$$\begin{pmatrix} -\Gamma^l_a & C^l_{ab} \\ -C^l_{ba} & -\Gamma^l_b \end{pmatrix}.$$

One gets the amplitude $\ell$ of the $l_a$ component of the Neel vector:

$$\ell = \frac{\gamma M_0 L_0 W_0 \sqrt{\Omega^2 + \left(\Gamma^l_b\right)^2}}{\sqrt{(\Omega^2 - \omega^2)^2 + 4\Gamma^2 \Omega^2}}, \tag{8}$$

where $\omega = |\omega_l| = \sqrt{(1+\alpha^2) C^l_{ab} C^l_{ba}}$ and $\Gamma = \mathrm{Im}(\omega_l) = (\Gamma^l_a + \Gamma^l_b)/2$.

## III. RESULTS

Below we investigate the dependence of $\ell$ on the acoustic wave frequency $\Omega$. To be specific, we consider the longitudinal LP2 phonons propagating along the $a$ axis and take $W = 0.1 J_0$ as an upper estimate of the driving amplitude. This choice corresponds to a strain amplitude of about 0.1%, which is experimentally achievable and remains well below the 0.7%–1.2% strain at which switching of the interlayer magnetic order from AFM to FM was observed [20].

The resulting $\ell(\Omega)$ dependence predicted by Eq. (8) is shown in Fig. 3 for different values of the magnetic field. It clearly demonstrates the resonant nature of the phonon-assisted magnon generation mechanism. This linearized model predicts that the resonant oscillation amplitude of $l_a$ can reach 0.2, while the maximum possible value of $|l_a|$ is 2. To confirm the results of the analytical model, we performed a numerical simulation of the LLG equations [35]. The simulation was carried out on a one-dimensional uniform grid. We have considered the following magnetic field values: $0.2B_c$, $0.4B_c$, $0.6B_c$, $0.8B_c$, and $0.95B_c$. In each field, we varied the frequency of the exciting phonon from 5 to 30 GHz with the 5 GHz step. The values of the $l_a$ amplitude established after a 32 ns long evolution, which is enough to reach a steady state, are shown in Fig. 3 with color dots. The analytical results demonstrate good agreement with simulations of the full LLG dynamics for the considered excitation amplitude.

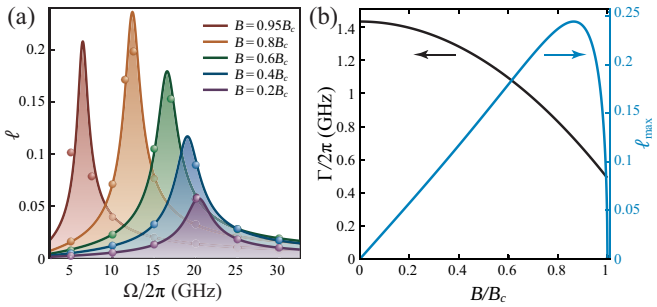



FIG. 3. (a) The amplitude $\ell$ of the $l_a$ component of the IP spin wave excited by the LP2 phonons as a function of the driving frequency at different magnetic field strengths. The driving strength amplitude is $0.1J_0$. The solid curves correspond to the predictions of the analytical model [see Eq. (8)], while the results of the numerical simulation of the LLG dynamics are shown with the dots of the same color. The peak structure of the response curves indicates the resonant nature of the phonon-driven magnon generation in CrSBr bilayers. The resonance frequency decreases with increasing magnetic field in accordance with Fig. 2(d). (b) Left axis: The decay rate $\Gamma = \mathrm{Im}(\omega_l)$ of the IP magnon mode at the resonance with LP2 phonons. This value characterizes a half-width of the resonance contours shown in panel (a). Right axis: the peak oscillating amplitude $\ell_{\max}$ vs magnetic field strength.

The dependence of the peak generation amplitude and half-width of a resonant generation contour on the external magnetic field is shown in Fig. 3(b) with blue and black curves, right and left axes, respectively. Note that the maximum of the blue curve, corresponding to the magnetic field optimal for magnon generation, is shifted in the region of larger magnetic fields with respect to those that maximize the coupling strength between phonons and magnons $B = B_c/\sqrt{2}$, which is due to the decrease of the losses $\Gamma$ with the magnetic field, as shown by the black curve.

The proposed mechanism can be experimentally tested using time-resolved pump-probe spectroscopy, which has been successfully employed to detect magnon dynamics in two-dimensional magnets [24]. In the canted phase, the resonant modulation of interlayer exchange by an acoustic wave induces coherent oscillations of the Neel vector that modulate exciton energy via strong magnetoexciton coupling [24,36]. The change in exciton energy $\Delta E_{\mathrm{ex}}$ with a change in angle $\theta$ between $\mathbf{n}_1$ and $\mathbf{n}_2$ can be estimated as $\Delta E_{\mathrm{ex}} = \Delta E^0_{\mathrm{ex}} \cos^2 \theta/2$, where $\Delta E^0_{\mathrm{ex}} = 10\,\mathrm{meV}$ [10]. In the magnetic field $0.8B_c$ and with a phonon frequency of 12.5 GHz,

one obtains a modulation depth of 2.2 meV. These effects should appear as periodic variations in reflectivity or magneto-optical Kerr effect signals at the acoustic frequency. The disappearance of the response in the collinear AFM and FM phases would provide a distinctive signature of the mechanism.

Note that we considered an out-of-plane orientation of the magnetic field. However, the proposed mechanism will also work in the case of a field applied along an intermediate magnetic axis. Such a realization would require smaller magnetic fields due to the lower anisotropy constant.

## IV. CONCLUSIONS

We proposed a mechanism for the efficient resonant generation of magnons in CrSBr bilayers by acoustic waves, showing that the application of a magnetic field creates a canted magnetic phase that supports a forced magnetic oscillation mode. We demonstrated that the resonant frequency can be tuned in the range of 1–30 GHz. The creation of effective magnon sources can have a significant impact on the development of modern spintronics.

## ACKNOWLEDGMENTS

The calculations of the magnon modes and the magnetic dynamics were supported by the Russian Science Foundation Grant No. 25-72-20029. The DFT calculation of the elasticity tensor and the calculation of the phonon modes were supported by State Assignment No. FSER-2026-0011 within the framework of the national project "Science and Universities". A.S. thanks the "BASIS" Foundation (Project No. 25-1-5-89-1) for supporting the micromagnetic modeling.

## DATA AVAILABILITY

The data that support the findings of this article are not publicly available. The data are available from the authors upon reasonable request.

[1] K. S. Novoselov, A. K. Geim, S. V. Morozov, D. Jiang, Y. Zhang, S. V. Dubonos, I. V. Grigorieva, and A. A. Firsov, Electric field effect in atomically thin carbon films, Science **306**, 666 (2004).

[2] Y. Luo, J. Zhao, A. Fieramosca, Q. Guo, H. Kang, X. Liu, T. C. H. Liew, D. Sanvitto, Z. An, S. Ghosh, Z. Wang, H. Xu, and Q. Xiong, Strong light-matter coupling in van der Waals materials, Light: Sci. Appl. **13**, 203 (2024).

[3] W. Tang, H. Liu, Z. Li, A. Pan, and Y.-J. Zeng, Spin-orbit torque in van der Waals-layered materials and heterostructures, Adv. Sci. **8**, 2100847 (2021).

[4] B. Huang, G. Clark, E. Navarro-Moratalla, D. R. Klein, R. Cheng, K. L. Seyler, D. Zhong, E. Schmidgall, M. A. McGuire, D. H. Cobden, W. Yao, D. Xiao, P. Jarillo-Herrero, and X. Xu, Layer-dependent ferromagnetism in a van der Waals crystal down to the monolayer limit, Nature (London) **546**, 270 (2017).

[5] H. H. Kim, B. Yang, T. Patel, F. Sfigakis, C. Li, S. Tian, H. Lei, and A. W. Tsen, One million percent tunnel magnetoresistance in a magnetic van der Waals heterostructure, Nano Lett. **18**, 4885 (2018).

[6] S. Jiang, L. Li, Z. Wang, K. F. Mak, and J. Shan, Controlling magnetism in 2D $CrI_3$ by electrostatic doping, Nat. Nanotechnol. **13**, 549 (2018).

[7] Z. Sun, Y. Yi, T. Song, G. Clark, B. Huang, Y. Shan, S. Wu, D. Huang, C. Gao, Z. Chen, M. McGuire, T. Cao, D. Xiao, W.-T. Liu, W. Yao, X. Xu, and S. Wu, Giant nonreciprocal second-harmonic generation from antiferromagnetic bilayer $CrI_3$, Nature (London) **572**, 497 (2019).

[8] Y. Zhumagulov, S. Chiavazzo, I. A. Shelykh, and O. Kyriienko, Robust polaritons in magnetic monolayers of $CrI_3$, Phys. Rev. B **108**, L161402 (2023).

[9] B. Huang, M. A. McGuire, A. F. May, D. Xiao, P. Jarillo-Herrero, and X. Xu, Emergent phenomena and proximity effects in two-dimensional magnets and heterostructures, Nat. Mater. **19**, 1276 (2020).

[10] N. P. Wilson, K. Lee, J. Cenker, K. Xie, A. H. Dismukes, E. J. Telford, J. Fonseca, S. Sivakumar, C. Dean, T. Cao, X. Roy, X. Xu, and X. Zhu, Interlayer electronic coupling on demand in a 2D magnetic semiconductor, Nat. Mater. **20**, 1657 (2021).

[11] F. Wu, I. Gutiérrez-Lezama, S. A. López-Paz, M. Gibertini, K. Watanabe, T. Taniguchi, F. O. von Rohr, N. Ubrig, and A. F. Morpurgo, Quasi-1D electronic transport in a 2D magnetic semiconductor, Adv. Mater. **34**, 2109759 (2022).

[12] C. Boix-Constant, S. Mañas-Valero, A. M. Ruiz, A. Rybakov, K. A. Konieczny, S. Pillet, J. J. Baldoví, and E. Coronado, Probing the spin dimensionality in single-layer CrSBr van der Waals heterostructures by magneto-transport measurements, Adv. Mater. **34**, 2204940 (2022).

[13] K. Lee, A. H. Dismukes, E. J. Telford, R. A. Wiscons, J. Wang, X. Xu, C. Nuckolls, C. R. Dean, X. Roy, and X. Zhu, Magnetic order and symmetry in the 2D semiconductor CrSBr, Nano Lett. **21**, 3511 (2021).

[14] E. J. Telford, A. H. Dismukes, K. Lee, M. Cheng, A. Wieteska, A. K. Bartholomew, Y.-S. Chen, X. Xu, A. N. Pasupathy, X. Zhu, C. R. Dean, and X. Roy, Layered antiferromagnetism induces large negative magnetoresistance in the van der Waals semiconductor CrSBr, Adv. Mater. **32**, 2003240 (2020).

[15] Y. Wang, S.-S. Wang, Y. Lu, J. Jiang, and S. A. Yang, Strain-induced isostructural and magnetic phase transitions in monolayer $MoN_2$, Nano Lett. **16**, 4576 (2016).

[16] K. Bagani, A. Vervelaki, D. Jetter, A. Devarakonda, M. A. Tschudin, B. Gross, D. G. Chica, D. A. Broadway, C. R. Dean, X. Roy, P. Maletinsky, and M. Poggio, Imaging strain-controlled magnetic reversal in thin CrSBr, Nano Lett. **24**, 13068 (2024).

[17] E. Uykur, A. A. Tsirlin, F. Long, M. Wenzel, M. Dressel, K. Mosina, Z. Sofer, M. Helm, and S. Zhou, Phonon and magnon

dynamics across the antiferromagnetic transition in the two-dimensional layered van der Waals material CrSBr, Phys. Rev. B **111**, 174434 (2025).

[18] X. Xu, X. Wang, P. Chang, X. Chen, L. Guan, and J. Tao, Strong spin-phonon coupling in two-dimensional magnetic semiconductor CrSBr, J. Phys. Chem. C **126**, 10574 (2022).

[19] F. Fei, Y. Mao, W. Fang, W. Liu, J. P. Rollins, A. L. N. Kondusamy, B. Lv, Y. Ping, Y. Wang, and J. Xiao, Spin-mechanical coupling in 2D antiferromagnet CrSBr, Nano Lett. **24**, 10467 (2024).

[20] J. Cenker, S. Sivakumar, K. Xie, A. Miller, P. Thijssen, Z. Liu, A. Dismukes, J. Fonseca, E. Anderson, X. Zhu, X. Roy, D. Xiao, J.-H. Chu, T. Cao, and X. Xu, Reversible strain-induced magnetic phase transition in a van der Waals magnet, Nat. Nanotechnol. **17**, 256 (2022).

[21] N. Liu, C. Wang, Y. Zhang, F. Pang, Z. Cheng, Y. Zhang, and W. Ji, Intralayer strain tuned interlayer magnetism in bilayer CrSBr, Phys. Rev. B **109**, 214422 (2024).

[22] C. Kittel, Physical theory of ferromagnetic domains, Rev. Mod. Phys. **21**, 541 (1949).

[23] C. Kittel, Interaction of spin waves and ultrasonic waves in ferromagnetic crystals, Phys. Rev. **110**, 836 (1958).

[24] Y. J. Bae, J. Wang, A. Scheie, J. Xu, D. G. Chica, G. M. Diederich, J. Cenker, M. E. Ziebel, Y. Bai, H. Ren, C. R. Dean, M. Delor, X. Xu, X. Roy, A. D. Kent, and X. Zhu, Exciton-coupled coherent magnons in a 2D semiconductor, Nature (London) **609**, 282 (2022).

[25] J. Chen, K. Yamamoto, C. Kang, R. Yuan, K. Yu, C. Hu, J. Hu, L. Sheng, J. Wang, S. Liu, D. Yu, J.-P. Ansermet, Y.-J. Zeng, S. Maekawa, and H. Yu, Surface magnon propagation in a van der Waals antiferromagnet, Phys. Rev. Lett. **136**, 056702 (2026).

[26] Y. J. Bae, T. Handa, Y. Dai, J. Wang, H. Liu, A. Scheie, D. G. Chica, M. E. Ziebel, A. D. Kent, X. Xu, K. Shen, X. Roy, and X. Zhu, Transient magnetoelastic coupling in CrSBr, Phys. Rev. B **109**, 104401 (2024).

[27] X. Shen, J. Cao, B. Cong, B. Zou, W. Liang, Z. Peng, J. Zhao, and A. Kavokin, Electron-phonon coupling probed by ultrafast coherent phonon spectroscopy in bulk van der Waals CrSBr, Phys. Rev. B **113**, 125406 (2026).

[28] X. Shen, B. Cong, J. Cao, J. Huang, W. Liang, J. Zhao, and B. Zou, Orthogonal magnon-phonon coupling enables information encoding in bulk CrSBr, J. Phys. Chem. Lett. **16**, 12625 (2025).

[29] K. Yang, G. Wang, L. Liu, D. Lu, and H. Wu, Triaxial magnetic anisotropy in the two-dimensional ferromagnetic semiconductor CrSBr, Phys. Rev. B **104**, 144416 (2021).

[30] See Supplemental Material at http://link.aps.org/supplemental/10.1103/xdkq-h9km for the details of the parametrization of the continuous model, the derivation of the LLG equations, and the details of the DFT calculations, which also includes Refs. [37–43].

[31] T. M. J. Cham, D. G. Chica, X. Huang, K. Watanabe, T. Taniguchi, X. Roy, Y. K. Luo, and D. C. Ralph, Spin-filter tunneling detection of antiferromagnetic resonance with electrically tunable damping, Science **389**, 479 (2025).

[32] O. Göser, W. Paul, and H. Kahle, Magnetic properties of CrSBr, J. Magn. Magn. Mater. **92**, 129 (1990).

[33] N. Stetzuhn, A. M. Kumar, S. Kovalchuk, D. Yagodkin, L. Simon, S. Mañas-Valero, E. Coronado, T. Taniguchi, K. Watanabe, D. Gill, S. Sharma, P. W. Brouwer, C. von Korff Schmising, S. Eisebitt, and K. I. Bolotin, Tunable magnons in a dual-gated 2D antiferromagnet, Nat. Commun. **17**, 5262 (2026).

[34] H. Li, Y. Yang, Z. Xia, Y. Wang, J. Wei, J. He, and R. Wang, Stacking effects on magnetic, vibrational, and optical properties of CrSBr bilayers, Phys. Rev. B **111**, 125411 (2025).

[35] P. S. Shaban, I. S. Lobanov, V. M. Uzdin, and I. V. Iorsh, Skyrmion dynamics in moiré magnets, Phys. Rev. B **108**, 174440 (2023).

[36] G. M. Diederich, J. Cenker, Y. Ren, J. Fonseca, D. G. Chica, Y. J. Bae, X. Zhu, X. Roy, T. Cao, D. Xiao, and X. Xu, Tunable interaction between excitons and hybridized magnons in a layered semiconductor, Nat. Nanotechnol. **18**, 23 (2023).

[37] J. J. Mortensen, A. H. Larsen, M. Kuisma, A. V. Ivanov, A. Taghizadeh, A. Peterson, A. Haldar, A. O. Dohn, C. Schäfer, E. Jónsson, *et al.*, GPAW: An open Python package for electronic structure calculations, J. Chem. Phys. **160**, 092503 (2024).

[38] J. J. Mortensen, L. B. Hansen, and K. W. Jacobsen, Real-space grid implementation of the projector augmented wave method, Phys. Rev. B **71**, 035109 (2005).

[39] J. Enkovaara, C. Rostgaard, J. J. Mortensen, J. Chen, M. Dułak, L. Ferrighi, J. Gavnholt, C. Glinsvad, V. Haikola, H. A. Hansen, H. H. Kristoffersen, M. Kuisma, A. H. Larsen, L. Lehtovaara, M. Ljungberg, O. Lopez-Acevedo, P. G. Moses, J. Ojanen, T. Olsen, and V. Petzold, Electronic structure calculations with GPAW: A real-space implementation of the projector augmented-wave method, J. Phys.: Condens. Matter **22**, 253202 (2010).

[40] J. P. Perdew, K. Burke, and M. Ernzerhof, Generalized gradient approximation made simple, Phys. Rev. Lett. **77**, 3865 (1996).

[41] P. T. Jochym, Elastic, Release v5. 1.0-14-g6596fd4, 2018, https://wolf.ifj.edu.pl/~jochym/Elastic.pdf.

[42] P. T. Jochym, K. Parlinski, and M. Sternik, TiC lattice dynamics from *ab initio* calculations, Eur. Phys. J. B **10**, 9 (1999).

[43] P. T. Jochym and K. Parlinski, *Ab initio* lattice dynamics and elastic constants of ZrC, Eur. Phys. J. B **15**, 265 (2000).